Tunable Bandpass Filter With Two Adjustable Transmission Poles and Compensable Coupling

Xun Luo, *Senior Member, IEEE*, Sheng Sun, *Senior Member, IEEE*, and Robert Bogdan Staszewski, *Fellow, IEEE*

***Abstract*—In this paper, tunable microstrip bandpass filters with two adjustable transmission poles and compensable coupling are proposed. The fundamental structure is based on a half-wavelength ($\lambda/2$) resonator with a center-tapped open-stub. Microwave varactors placed at various internal nodes separately adjust the filter's center frequency and bandwidth over a wide tuning range. The constant absolute bandwidth is achieved at different center frequencies by maintaining the distance between the in-band transmission poles. Meanwhile, the coupling strength could be compensable by tuning varactors that are side and embedding loaded in the parallel coupled microstrip lines (PCMLs). As a demonstrator, a second-order filter with seven tuning varactors is implemented and verified. A frequency range of 0.58–0.91 GHz with a 1-dB bandwidth tuning from 115 to 315 MHz (i.e., 12.6%–54.3% fractional bandwidth) is demonstrated. Specifically, the return loss of passbands with different operating center frequencies can be achieved with same level, i.e., about 13.1 and 11.6 dB for narrow and wide passband responses, respectively. To further verify the etch-tolerance characteristics of the proposed prototype fitler, another second-order filter with nine tuning varactors is proposed and fabricated. The measured results exhibit that the tunable fitler with the embedded varactor-loaded PCML has less sensitivity to fabrication tolerances. Meanwhile, the passband return loss can be achieved with same level of 20 dB for narrow and wide passband responses, respectively.**

***Index Terms*—Bandpass filter, compensable coupling, parallel coupled microstrip line (PCML), tunable, varactor.**

I. Introduction

THE MODERN wireless communication systems require reconfigurability for a multi-mode and multi-band operation. Tunable RF bandpass filters, including microstrip filters with small size, are essential key components for practical RF front-ends and thus generate a great deal of research attention. The filters in [1] and [2] with loaded varactors are capable of tuning the center frequency of the passband and stopband. However, their absolute bandwidth increases rapidly for higher central resonant frequencies. In general, to maintain a constant passband/stopband bandwidth independent of the tuning frequency, the coupling coefficients must vary inversely with the tuning frequency. In [3], a varactor tuning combines bandpass filtering using step-impedance resonators so that the inter-resonator coupling could be controlled to meet the constant bandwidth with shorter electrical lengths of line elements. Meanwhile, in [4] and [5], p-i-n diodes are used to control the filter's central resonance, and varactors continuously adjust the bandwidth at the specific operating frequency. Besides, the bandwidth can be controlled at a fixed center frequency [6]–[8] or at different center frequencies [9], [10]. Moreover, some approaches using a few resonators, such as an open-stub resonator, a dual-mode resonator, and a multiple-mode resonator, are proposed to tune the bandwidth [11]–[21]. However, the coupling strength of passbands or stopbands seems to be always neglected during the design of the tunable filters, which sometimes results in invalid bands after adjustments for practical applications.

In this paper, a compact tunable microstrip bandpass filter is proposed based on a half-wavelength ($\lambda/2$) resonator with an open-stub tapped at its center. The center-tapped open-stub can not only contribute two transmission poles in conjunction with the $\lambda/2$ resonator, but also create a single transmission zero at a particular frequency. Locations of the two transmission poles are theoretically analyzed and parallel-coupled microstrip lines (PCMLs) with loaded varactors are investigated to demonstrate the distributed coupling performance in terms of a J-inverter susceptance. Based on the analysis, a detailed design procedure of the tunable filter is proposed and then experimentally verified. Measurements show that the filters keep the absolute bandwidth constant over different center frequencies, but can also compensate for the passband coupling strength variation.

II. Tunable Bandpass Filter Schematic and Operation

Fig. 1 shows a configuration of the tunable bandpass filter. It consists of a $\lambda/2$ resonator with an open-stub tapped at its center and two $\lambda/4$ PCMLs connected to the input/output (I/O) ports. Tuning varactors are connected at various internal nodes: C_1 and C_2 tapped at the open-stub and $\lambda/2$ resonator, respectively, and $C_{31,32...,3n}$ are embedded in the $\lambda/4$ PCMLs. Sections II-A–II-E investigate the characteristics and mechanism of the proposed filter.

A. Mechanism of Stub-Tapped Bandpass Filter

Fig. 2 depicts a configuration of the conventional stub-tapped bandpass filter [22], [23], which is a second-order filter. Physical

Manuscript received March 26, 2014; revised June 10, 2014; accepted June 23, 2014. Date of publication July 22, 2014; date of current version September 02, 2014. This work was supported by the Huawei Technologies Company Ltd. and Hong Kong Grant GRF 716112.

X. Luo was with the Microwave Branch, 2012 Laboratory, Huawei Technologies Company Ltd., 518129 Shenzhen, China. He is now with EWI, Delft University of Technology, 2628CD Delft, The Netherlands (e-mail: xun-luo@ieee.org).

S. Sun is with the Department of Electrical and Electronic Engineering, The University of Hong Kong, Hong Kong (e-mail: sunsheng@ieee.org).

R. B. Staszewski is with EWI, Delft University of Technology, 2628CD Delft, The Netherlands.

Color versions of one or more of the figures in this paper are available online at http://ieeexplore.ieee.org.

Digital Object Identifier 10.1109/TMTT.2014.2337287

0018-9480 © 2014 IEEE. Translations and content mining are permitted for academic research only. Personal use is also permitted, but republication/redistribution requires IEEE permission. See http://www.ieee.org/publications_standards/publications/rights/index.html for more information.

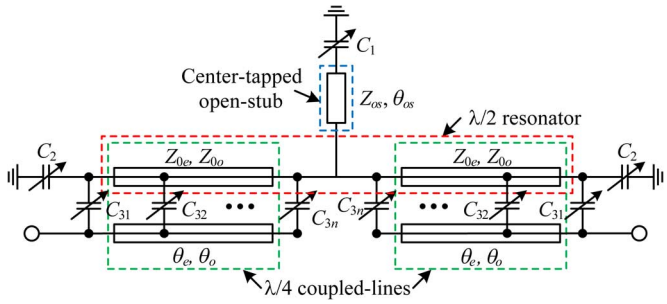

Fig. 1. Configuration of the proposed tunable bandpass filter.

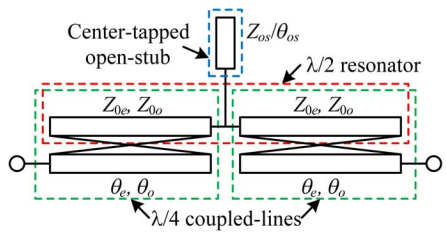

Fig. 2. Configuration of a conventional stub-tapped bandpass filter.

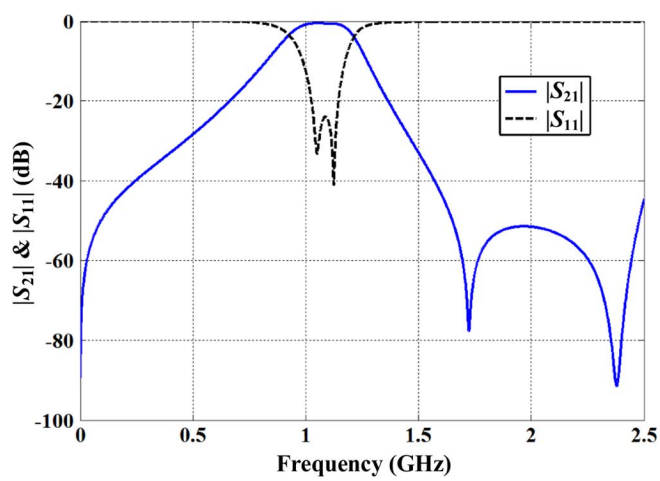

Fig. 3. Frequency response of the conventional stub-tapped bandpass filter.

length of the open-stub tapped at the center of the $\lambda/2$ resonator can be changed to adjust the notch frequency in the stopband. As the characteristic impedance $Z_{os} = 1/Y_{os}$ increases, the transmission zero is located closer to the passband edge. Once the length of the center-tapped open-stub is shorter than $\lambda/4$, the transmission zero is then placed on the right side of the transmission pole allocated by the $\lambda/2$ resonator and open-stub [24]. For the bandpass filter design, the characteristic impedances, i.e., $Z_1 = 1/Y_1$ and Z_{os} of the resonator and open-stub, respectively, are selected by the location of transmission poles as well as the filter bandwidth, and the frequency of the transmission zero is defined by the electrical length of the open-stub. Here, the center-tapped open-stub is constructed slightly shorter than $\lambda/4$ at the center frequency to make the transmission zero implemented at the upper stopband, as depicted in Fig. 3. The proposed filter is designed to have a fractional bandwidth (FBW) of nearly 25% and its central frequency at 1.1 GHz with a passband return loss more than 20 dB.

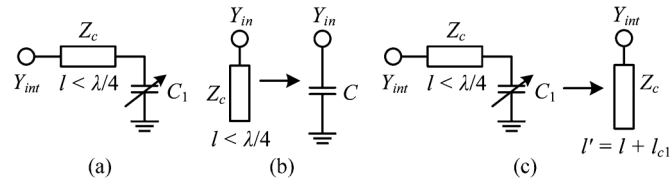

Fig. 4. (a) Varactor-loaded open-stub. (b) Open-stub equivalence. (c) Equivalent model of the varactor-loaded open-stub.

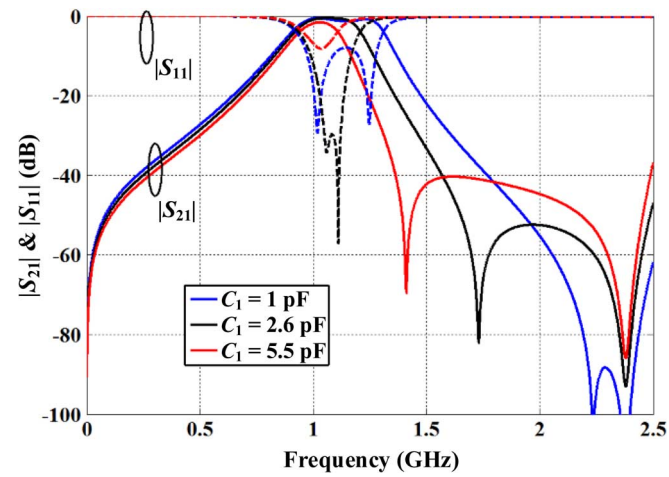

Fig. 5. Effects of the varactor-loaded open-stub on the frequency response of stub-tapped bandpass filter.

B. Varactor-Loaded Open-Stub

As mentioned above, adjusting the length of the open-stub can vary the location of the right-side transmission pole. Here, a varactor C_1 is added between the open-stub and ground, as shown in Fig. 4(a). It is well known that a microstrip open-stub can be equivalent to a shunt capacitor [25], as shown in Fig. 4(b), whose input admittance is

$$Y_{\text{in}} = jY_{os} \tan\left(\frac{2\pi}{\lambda} l\right) \tag{1}$$

where l is the physical length of the open-stub. If $l < \lambda/4$, the input admittance is capacitive with an equivalent value of

$$C = \frac{Y_{os} \tan\left(\frac{2\pi}{\lambda} l\right)}{2\pi f} \tag{2}$$

Thus, the capacitor and open-stub can be equivalently converted to each other. The modified length l' of the varactor-loaded open-stub can then be expressed as

$$l' = l + \frac{\arctan(Z_{os} C_1 2\pi f)}{2\pi} \lambda. \tag{3}$$

Equation (3) can be utilized to investigate the effect of the tuning varactor on the frequency response. Fig. 5 reveals that increasing the capacitance from 1 to 5.5 pF not only lowers the transmission zero, but also degrades the coupling strength of the passband around the resonances.

C. Varactor-Loaded PCML

To compensate for the above degradation of the coupling strength of passband, various varactor-loaded PCMLs are introduced in Fig. 6. To analyze the characteristics of the

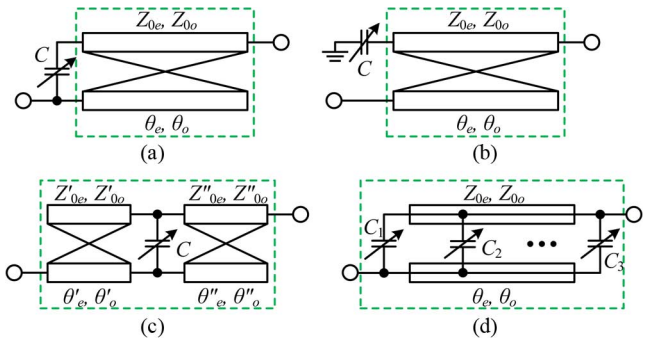

Fig. 6. Varactor-loaded PCMLs. (a) Shunt varactor-loaded PCML. (b) Series varactor-loaded PCML. (c) Embedded varactor-loaded PCML. (d) Array varactor-loaded PCML.

varactor-loaded PCMLs, the $ABCD$-matrix calculated from the boundary conditions is introduced. Here, for example, the $ABCD$-matrix of the shunt varactor-loaded PCML shown in Fig. 6(a) is expressed as follows:

$$A = \frac{\cos\theta_e\cos\theta_o + \frac{1}{2}jZ(\cos\theta_e\sin\theta_o Y_{0o} + \cos\theta_o\sin\theta_e Y_{0e})}{\cos\theta_o - \frac{1}{2}jZ(\sin\theta_e Y_{0e} - \sin\theta_o Y_{0o})} \tag{4}$$

$$\begin{aligned} B = &\frac{\frac{1}{2}Z(1+\cos\theta_e\cos\theta_o)}{\cos\theta_o - \frac{1}{2}jZ(\sin\theta_e Y_{0e} - \sin\theta_o Y_{0o})} \\ &- \frac{\frac{1}{4}(Z_{0e}Y_{0o}\sin\theta_e\sin\theta_o - Z_{0o}Y_{0e}\sin\theta_e\sin\theta_o)}{\cos\theta_o - \frac{1}{2}jZ(\sin\theta_e Y_{0e} - \sin\theta_o Y_{0o})} \\ &+ \frac{\frac{1}{2}j(Z_{0o}\cos\theta_e\sin\theta_o + Z_{0e}\cos\theta_o\sin\theta_e)}{\cos\theta_o - \frac{1}{2}jZ(\sin\theta_e Y_{0e} - \sin\theta_o Y_{0o})} \end{aligned} \tag{5}$$

$$C = \frac{j\sin\theta_e Y_{0e}(2\cos\theta_o + jZ\sin\theta_o Y_{0o})}{\cos\theta_o - \frac{1}{2}jZ(\sin\theta_e Y_{0e} - \sin\theta_o Y_{0o})} \tag{6}$$

$$D = \frac{j\sin\theta_e Y_{0e}\left(j\sin\theta_o Z_{0o} + \frac{1}{2}Z(\cos\theta_e + \cos\theta_o)\right)}{\cos\theta_o - \frac{1}{2}jZ(\sin\theta_e Y_{0e} - \sin\theta_o Y_{0o})} + \cos\theta_e \tag{7}$$

where $Z = -j/\omega C$ and $Z_{0o,e}$, $Y_{0o,e}$, and $\theta_{o,e}$ are the relevant parameters of the PCML. For further derivation about the $ABCD$-matrix for other blocks of Fig. 6 shown, please refer to Appendix A. Based on the $ABCD$-matrix of the structure, the two-port admittance π-model can then be derived. This model could be further simplified into a susceptance π-model if the lossless case is assumed [26]. Besides, considering the scheme shown in Fig. 6(a) being asymmetric, then the model could be transformed to the J-inverter topology consisting of a susceptance with two transmission lines (i.e., Y_1/θ_1 and Y_2/θ_2) [27], as shown in Fig. 7,

$$\overline{J} = \frac{J}{\sqrt{Y_1 Y_2}} = \frac{\sin\left(-\frac{\phi_1}{2}\right) + \overline{B_{11}}\cos\left(-\frac{\phi_1}{2}\right)}{\overline{B_{12}}\sin\left(-\frac{\phi_2}{2}\right)} \tag{8}$$

$$\phi_1 = M_1\pi + \arctan\left(\frac{2\left(\overline{B_{11}} + \overline{B_{22}}|\overline{B}|\right)}{1 + \overline{B_{22}}^2 - \overline{B_{11}}^2 - |\overline{B}|^2}\right) \tag{9}$$

$$\phi_2 = M_2\pi + \arctan\left(\frac{2\left(\overline{B_{22}} + \overline{B_{11}}|\overline{B}|\right)}{1 + \overline{B_{11}}^2 - \overline{B_{22}}^2 - |\overline{B}|^2}\right) \tag{10}$$

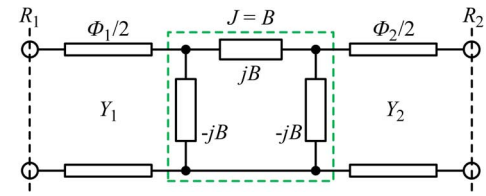

Fig. 7. Equivalent J-inverter topology of the structure in Fig. 6(a).

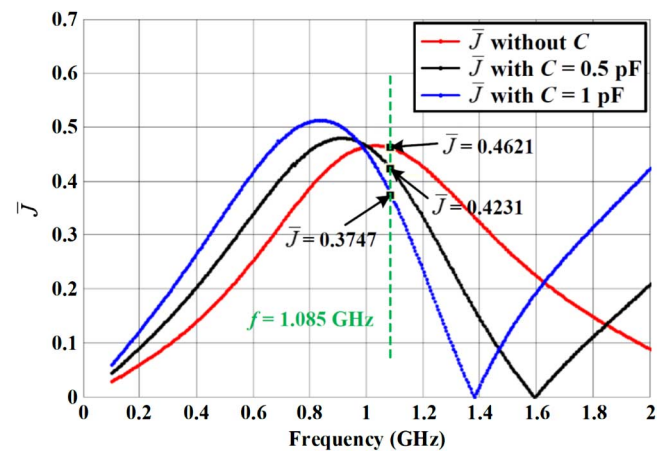

Fig. 8. Effects of the varactor on the normalized J-inverter susceptance $\overline{J}$ refer to the structure in Fig. 6(a).

where $\overline{B_{11}} = B_{11}/Y_1$, $\overline{B_{22}} = B_{22}/Y_2$, $\overline{B_{12}} = B_{12}/\sqrt{Y_1 Y_2}$, $|\overline{B}| = \overline{B_{11}B_{22}} - \overline{B_{12}}^2$, and $M_{1,2}$ are two positive integers and $\overline{J}$ is the normalized J-inverter susceptance. Fig. 8 depicts the various cases of $\overline{J}$ calculated from the shunt varactor-loaded PCML. It is shown that the trend of the $\overline{J}$ curve shifts lower as the capacitance increases [i.e., marked by the green dotted line (in online version)]. Therefore, it can be concluded that the coupling strength could be adjusted by tuning the varactor for the specific operating frequency. For practical applications, the effects of the varactor on even and odd modes should be considered. For the even mode, the varactor has no effect on the overall capacitance between the strip and ground because one of the varactor ends is an open circuit. Meanwhile, for the odd mode, the varactor is in parallel with the capacitance (i.e., $C_{\rm eq}$) between the strip and ground conductors. Therefore, once the varactor value increases, the overall capacitance $C_{\rm eq}$ increases, and thus the phase velocity of the odd mode is reduced, which causes a shift of the PCML resonance. Fig. 9 shows the effects of the varator on S-parameters. It is notable that the peak point of the coupling strength happens at the PCML resonant frequency and shifts lower as the varactor increases.

D. Combined Varactor-Loaded Open-Stub and PCML

Fig. 10 shows the combined varactor-loaded open-stub and PCML with varactors C_1 and C_2. From the boundary conditions for the PCML [24], the two-port network of the scheme is derived, then the $ABCD$-matrix is calculated as

$$A = \frac{1}{2}\frac{(2g_3 - Z_{c2}g_1)\cos\theta_e - 2Z_{c2}g_1\cos\theta_o - 2jZ_{0o}g_1\sin\theta_o}{g_3} \tag{11}$$

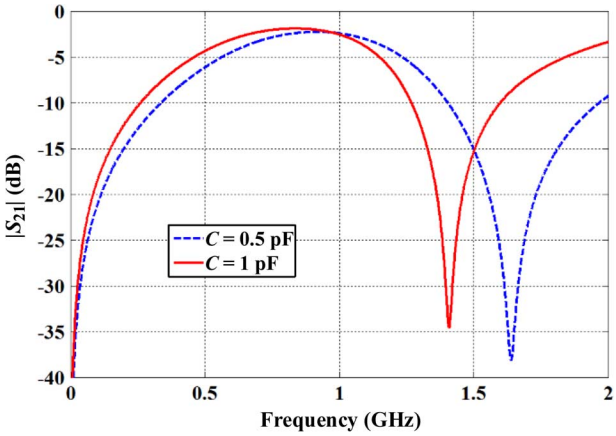

Fig. 9. Effects of the varactor on resonant frequency shifting.

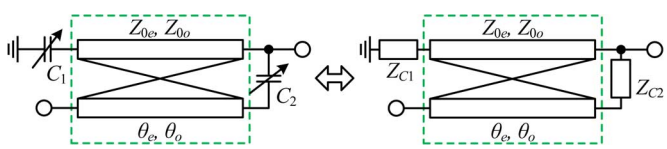

Fig. 10. Configuration of the combined varactor-loaded open-stub and PCML.

$$B = \frac{1}{2}\frac{Z_{c2}(g_2+g_3)(\cos\theta_e+\cos\theta_o)}{g_3} + \frac{j}{2}\frac{2Z_{0o}\left(g_2+\frac{1}{2}g_3\right)\sin\theta_o + Z_{0e}g_3\sin\theta_e}{g_3} \tag{12}$$

$$C = \frac{\cos\theta_o}{g_3} - \frac{1}{2}\frac{j\left(Y_{0e}(Z_{c2}g_1-2g_3)\sin\theta_e + Y_{0o}Z_{c2}g_1\sin\theta_o\right)}{g_3} \tag{13}$$

$$D = \frac{1}{2}\frac{(2g_2+g_3)\cos\theta_e + g_3\cos\theta_e}{g_3} + \frac{j}{2}\frac{(g_2+g_3)Z_{c2}(Y_{0e}\sin\theta_e + Y_{0o}\sin\theta_o)}{g_3} \tag{14}$$

$$g_1 = -\cos\theta_e + jY_{0e}Z_{c1}\sin\theta_e \tag{15}$$

$$g_2 = \frac{1}{2}(Z_{c1}-Z_{c2})(\cos\theta_o-\cos\theta_e) - \frac{j}{2}(Y_{0e}Z_{c1}Z_{c2}-Z_{0e})\sin\theta_e - \frac{j}{2}(Y_{0o}Z_{c1}Z_{c2}-Z_{0o})\sin\theta_o \tag{16}$$

$$g_3 = \frac{1}{2}(Z_{c2}\cos\theta_o - Z_{c2}\cos\theta_e - 2Z_{c1}\cos\theta_o) - \frac{j}{2}\left((Y_{0o}\sin\theta_o - Y_{0e}\sin\theta_e)Z_{c1}Z_{c2} - 2Z_{0o}\sin\theta_o\right) \tag{17}$$

where Z_{c1} and Z_{c2} are impedances of C_1 and C_2, respectively. Similarly to the analysis in the previous section, the normalized J-inverter susceptance $\overline{J}$ can be derived and the effect of varactor $\overline{J}$ is illustrated in Fig. 11. It is notable that the parameter $\overline{J}$ increases up to the maximum value first and then decreases as a nonmonotonic function of the frequency over 0.7–1.1 GHz for all the cases. The typical points with maximum $\overline{J}$ of each case are studied to show the effects created by C_1 and C_2. Two interesting effects can be found. The first effect is that once we

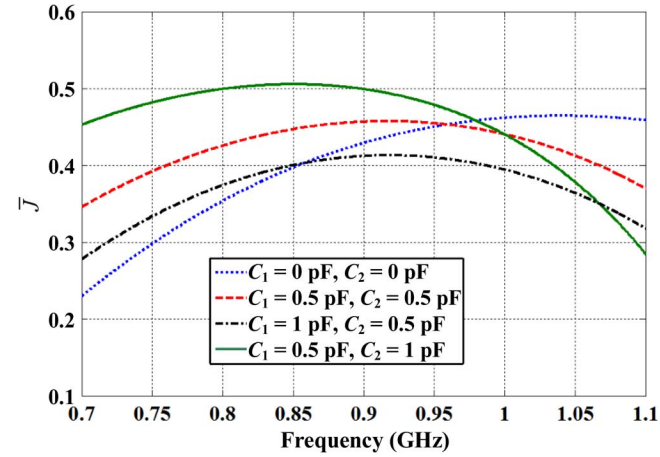

Fig. 11. Effects of the varactor on normalized J-susceptance $\overline{J}$.

set $C_2 = 0.5$ pF and then increase C_1 from 0.5 to 1 pF, the $\overline{J}$ value of maximum point decreases from 0.46 to 0.415 at the same frequency 920 MHz. The second effect is that once we set $C_1 = 0.5$ pF and increase C_2 from 0.5 to 1 pF, the maximum point of $\overline{J}$ changes from 920 MHz with 0.46 to 850 MHz with 0.506. From these effects, it is important to notice that the coupling strength of the structure not only can become weaker with increasing C_1, but also can be enhanced with incresing C_2. Thus, the coupling strength can be effectively compensated and kept invariant throughout various frequencies by properly tuning C_1 and C_2.

E. Design Example Investigation

Based on the aforementioned structures, four cases are investigated now for practical tunable bandpass filter designs. Case I is the filter consisting of a series varactor-loaded PCML and center-tapped varactor-loaded open-stub, as depicted in Fig. 12(a). Case II is the filter consisting of the shunt varactor-loaded PCML and center-tapped varactor-loaded open-stub, as illustrated in Fig. 12(b). Case III is the tunable bandpass filter shown in Fig. 12(c) with combined structures of Case I and Case II. Case IV is the tunable bandpass filter shown in Fig. 1. For all the cases in Fig. 12, the $ABCD$-matrix can be expressed as follows:

$$\begin{bmatrix} A & B \\ C & D \end{bmatrix} = \begin{bmatrix} A_1 & B_1 \\ C_1 & D_1 \end{bmatrix} \times \begin{bmatrix} 1 & -jZ_2\cot(\theta_c+\theta_{os}) \\ 0 & 1 \end{bmatrix} \begin{bmatrix} D_1 & B_1 \\ C_1 & A_1 \end{bmatrix} \tag{18}$$

where the first and third $ABCD$-matrices are derived from the varactor-loaded PCMLs, and the middle one is for the center-tapped varactor-loaded open-stub. To maintain the bandwidth of the tunable bandpass filter over various center frequencies, the structure in Case II is introduced and investigated. To theoretically derive C_1, the model as illustrated in Fig. 12 is equivalently expressed as in Fig. 13. Since the structure is symmetrical, the odd- and even-mode analysis of the center section in Fig. 13 can be adopted to characterize it, as depicted in Fig. 13(b) and (c). Therefore, the fundamental resonance f_e and f_o can be derived for the center section. For

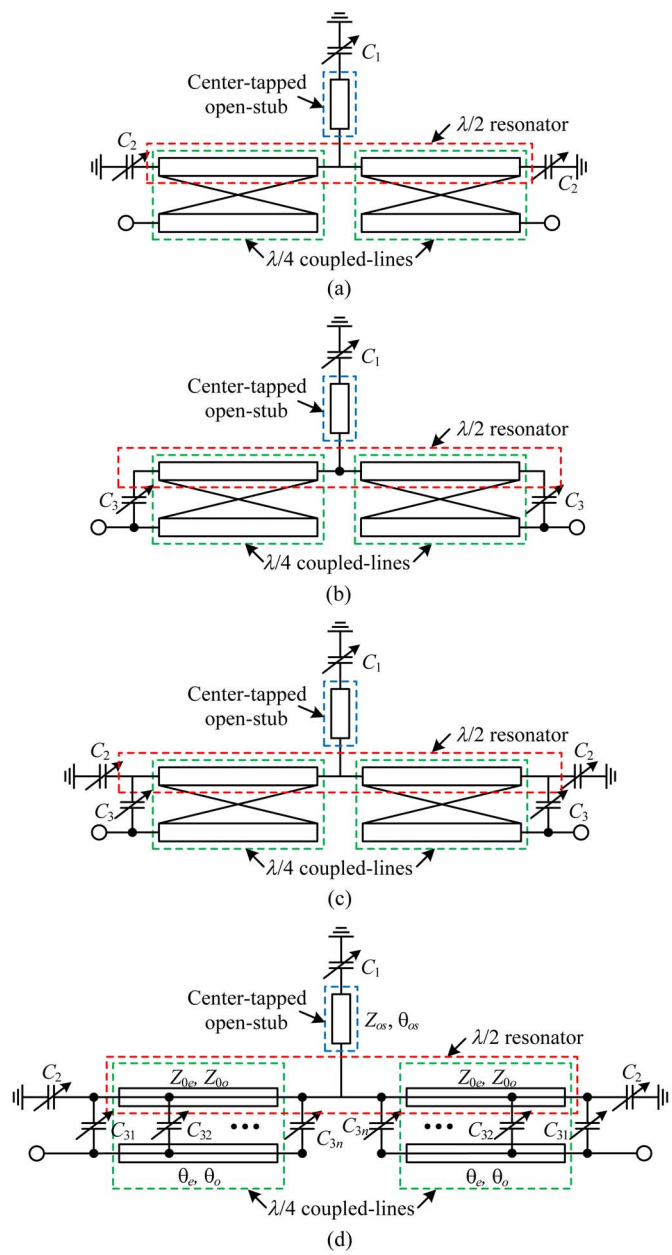

Fig. 12. Configurations of the tunable bandpass filter. (a) Case I. (b) Case II. (c) Case III. (d) Case IV.

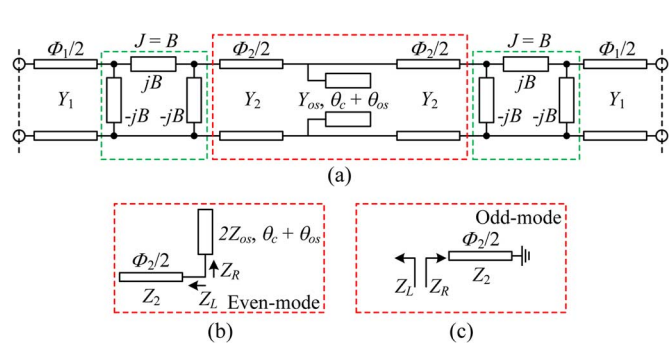

Fig. 13. (a) Equivalent model of Fig. 12. (b) Even mode of the center section. (c) Odd mode of the center section.

the even mode at resonance f_e, the input impedances Z_L and Z_R must satisfy the following requirement:

$$Z_L + Z_R = 0 \tag{19}$$

and thus,

$$2Z_{os}\cot(\theta_c + \theta_{os}) + Z_2 \cot\frac{\phi}{2} = 0. \tag{20}$$

For the odd mode, the resonant frequency f_o can be determined by

$$Z_2 \tan\frac{\phi}{2} = 0 \tag{21}$$

The central frequency f_0 of passband can then be expressed as

$$f_0 = \sqrt{f_e f_o} \tag{22}$$

which is assumed to be the center frequency between the two transmission poles. From (21), the lower transmission pole is determined by the odd mode. Once the desired odd mode is chosen by adjusting C_2 of the series varactor-loaded PCML, the upper transmission pole introduced by the even mode can then be tuned by varactor C_1 shown in Fig. 12(a). Thus far, the lower and upper transmission poles can be easily tuned. Therefore, since the varactors C_1 and C_2 tune the capacitance simultaneously, the adjusted center frequency with constant bandwidth can be easily achieved, as depicted in Fig. 14. However, the return loss of different passbands is not easily established at the same level in Case I. Fig. 8 suggests that it is possible to get the same $\overline{J}$ at the same frequency by tuning the varactor C_3. Nevertheless, that frequency is actually not the center frequency because of the overall passband changes introduced by the adjusted C_3. Therefore, C_1 should be adjusted to set the normalized value to be the same as the previous value at one frequency. Meanwhile, the frequency is just the current central frequency while C_3 has been fixed to the new value. For instance, the return loss of the original passband is 20 dB and the return loss of the new passband after tuning should be 20 dB. Based on the equations investigated above, the S_{11} related to C_1, C_3, and f_0 can be expressed as

$$20\log_{10}\left(abs\left(S_{11}(C_1, C_3, f_0)\right)\right) = -20 \text{ dB}. \tag{23}$$

Thus, based on (20)–(23), C_3 in Case II could be derived. For instance, once C_1 is set to 0.6 pF, C_3 could be calculated and optimized as 7.8 pF. In this way, the return loss can be tuned to the same level; however, the bandwidth cannot be kept the same, as shown in Fig. 15. Thus, to simultaneously achieve the equal coupling strengths and the constant bandwidth for the various center frequencies, the scheme depicted in Case III is implemented to achieve the frequency responses shown in Fig. 16. However, to design the tunable bandpass filter with much more flexibility, both the tunable transmission poles and compensable coupling are required. Therefore, Case IV in Fig. 12 is introduced. To clarify the selection of voltages to tune the varactors, the filter design procedure is summarized in a flowchart in Fig. 17. The first step is to design a fixed filter for a specific application with an acceptable performance [23]. The second step is to determine

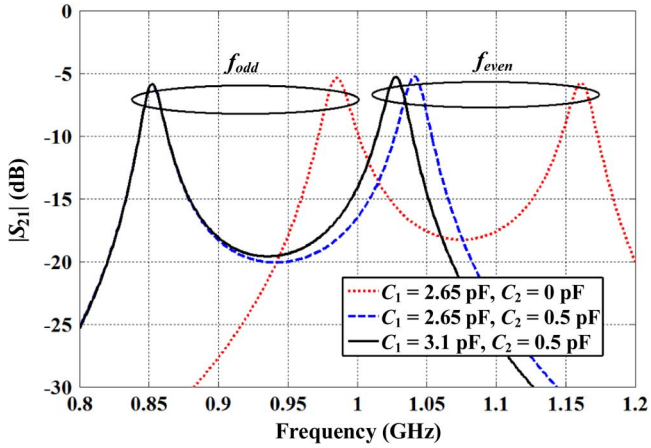

Fig. 14. Effects of C_1 and C_2 on bandwidth at various center frequencies.

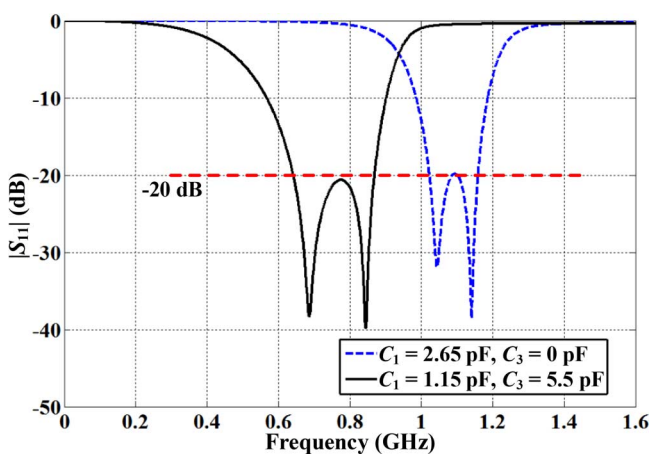

Fig. 15. Return loss $|S_{11}|$ with various varactors C_1 once C_3 is fixed in Case II of Fig. 12.

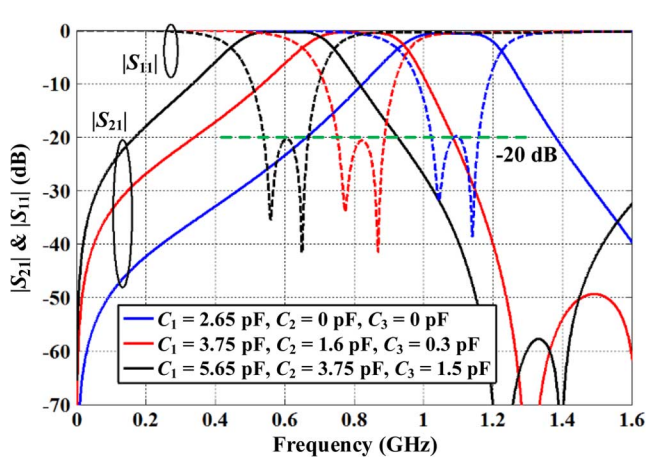

Fig. 16. Return loss $|S_{11}|$ with tunable varactors C_1, C_2, and C_3 in Case III of Fig. 12.

the capacitance of the varactors based on the desired requirements of the tunable frequency range and adjusted bandwidth. Based on the above analysis, it is notable that once the desired center frequency and bandwidth are given, the capacitance of varactors can be determined using the above-derived equations and design graphs.

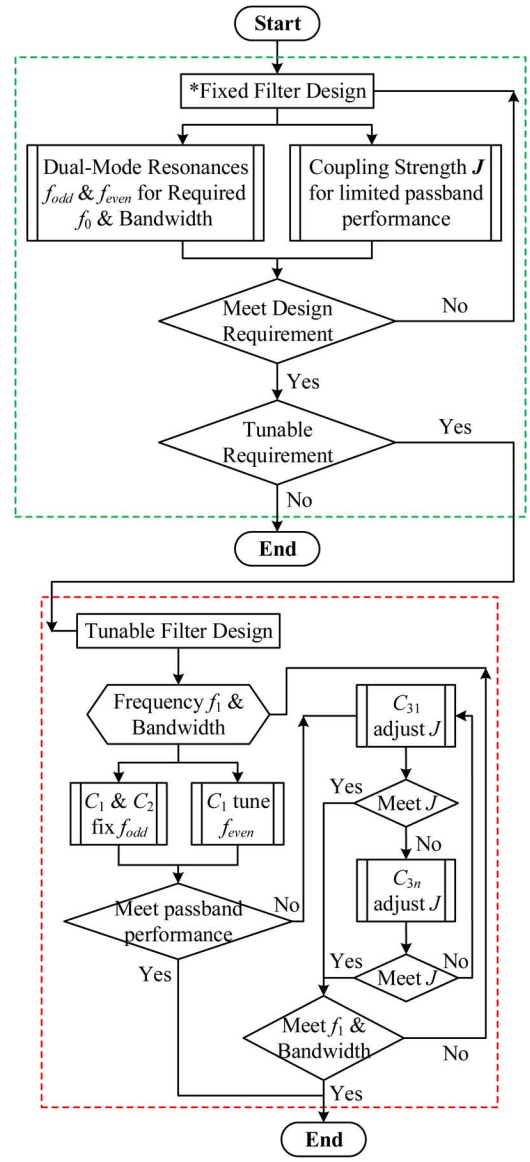

Fig. 17. Flowchart of the tunable filter design. (refer to [23] for a detailed design procedure of a fixed filter).

III. Filter Design and Experimental Results

A. Design I

Based on the above investigation, a tunable bandpass filter (i.e., Filter I) is proposed, implemented, and fabricated on a Rogers 4350B substrate of thickness $h = 0.508$ mm and $\epsilon_r = 3.66$. The configuration of the fabricated filter is shown in Fig. 18. The varactors (BB857) with adjustable range of about 0.52–6.6 pF for variable voltage in the 0–28-V interval are used. Five different dc voltages (i.e., V_1, V_2, V_{31}, V_{32}, and V_G) are used to achieve direct tuning of the varactors. They are isolated from each other by three dc blocks. The parasitic effects of the voltage supplies are isolated with a biasing circuit. For varactors C_1 and C_2, whose one end shares the ground with the microstrip filter, another biasing circuit is used, just replacing the series inductor with capacitor $C = 12$ pF in parallel. C_{31} and C_{32} varactors use a simple biasing circuit consisting of the RF choke (i.e., 2.2-μH inductor), which separates the dc power

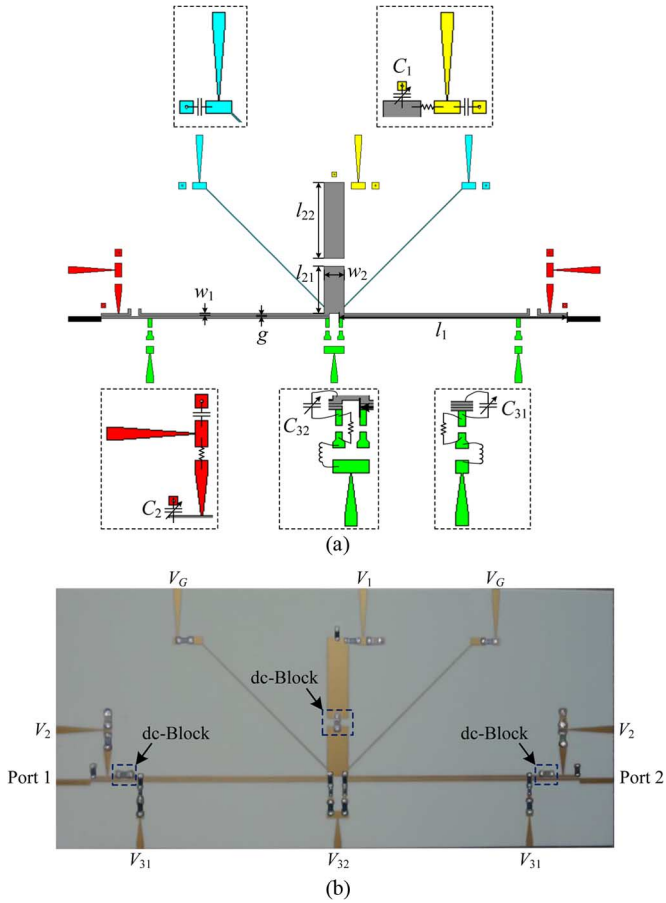

Fig. 18. Configuration of the proposed tunable bandpass filter (i.e., Filter I). (a) Implementation ($g = 0.15$ mm, $l_1 = 48.2$ mm, $l_{21} = 10$ mm, $l_{22} = 16.15$ mm, $w_1 = 0.45$ mm, and $w_2 = 4.2$ mm). (b) Fabrication.

from high frequency, and a resistance R of 10 kΩ, which is utilized to limit the bias current. Note that, for the symmetry sake, the dc voltage source (i.e., V_G) is applied to vary the reverse bias to control the varactor, which is implemented as a dual-tapped structure. The experimental performance of the proposed tunable bandpass filter is presented in Figs. 19 and 20. A frequency range of 0.58–0.91 GHz with a 1-dB bandwidth tuned between 115–315 MHz (i.e., 12.6%–54.3% FBW) is demonstrated. The typical insertion losses for the narrow and wide passband responses are 1.53 and 1.19 dB, respectively. Note that two interesting effects are considered for the passband return loss with the same level of various operated center frequencies. The first one is the mismatch of the symmetrical scheme after the soldering of the varactors, dc block, and bias components, which leads to imbalance of the tuning effects for the left and right part of the proposed filter. The second one is the capacitors for the dc block between the adjacent varactor bias circuits, which can introduce the interferences on the return loss level of different passbands. After optimization, the return loss level of the passbands with different operated center frequency in Fig. 19 and Fig. 20 can then be achieved to be 13.1 and 11.6 dB for the narrow and wide passband responses, respectively. Table I compares the tunable bandpass filters in this work to some tunable filters recently reported in the literature [15], [16], [18], [19], [21]. It

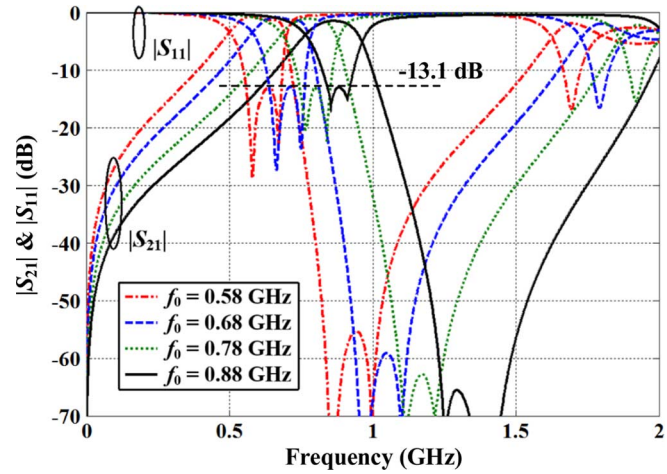

Fig. 19. Experimental results of the varactor-tuned bandpass filter (i.e., Filter I) with narrow passband responses. (Red line (in online version): $V_1 = 3.9$ V, $V_2 = 28$ V, $V_{31} = 28$ V, $V_{32} = 28$ V; Blue line (in online version): $V_1 = 3.1$ V, $V_2 = 10$ V, $V_{31} = 28$ V, $V_{32} = 18$ V; Green line (in online version): $V_1 = 2.05$ V, $V_2 = 6$ V, $V_{31} = 28$ V, $V_{32} = 5.5$ V; Black line: $V_1 = 1$ V, $V_2 = 4.25$ V, $V_{31} = 28$ V, $V_{32} = 3.8$ V.)

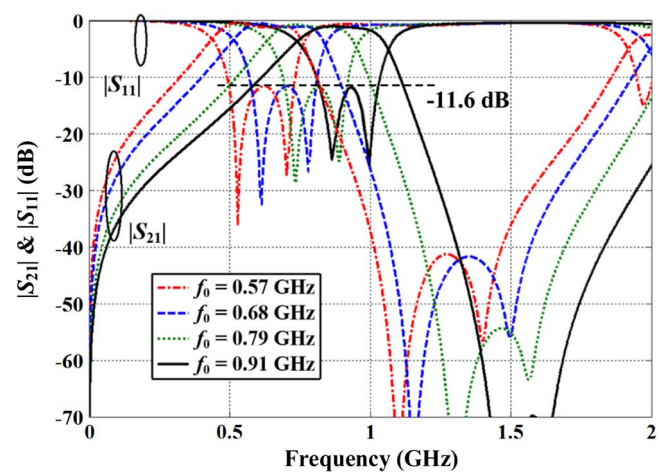

Fig. 20. Experimental results of the varactor-tuned bandpass filter (i.e., Filter I) with wide passband responses. (Red line (in online version): $V_1 = 28$ V, $V_2 = 28$ V, $V_{31} = 28$ V, $V_{32} = 28$ V; Blue line (in online version): $V_1 = 13.5$ V, $V_2 = 11$ V, $V_{31} = 10$ V, $V_{32} = 28$ V; Green line (in online version): $V_1 = 8$ V, $V_2 = 6.75$ V, $V_{31} = 5$ V, $V_{32} = 28$ V; Black line: $V_1 = 5.85$ V, $V_2 = 5$ V, $V_{31} = 2.45$ V, $V_{32} = 28$ V.)

can be concluded that the performance of our design based on two adjustable transmission poles and compensable coupling is competitive among the reported research works and attractive for practical application.

B. Design II

In practical applications, due to the imperfections of the fabrication process, frequency responses of filters are usually affected by the manufacturing tolerance [28]. For a constant amount of etching error, the varied widths of the strip and gap in the PCML can largely perturb the coupling strength of coupled lines [29]. Therefore, a compensable method should be developed to further address this mismatching problem. Consequently, in this paper, to further demonstrate the flexibility of the coupling compensation about embedded varactor-loaded PCMLs and array varactor-loaded PCMLs, the second-order

TABLE I
COMPARISONS OF MEASUREMENT WITH OTHER TUNABLE FILTERS

Ref	Frequency tuning Range (GHz)	BW tuning Range (MHz)	Insertion Loss (dB)	Return Loss (dB)	Number of tuning elements	Filter Order
*	**0.59-0.88** **0.59-0.905**	**115** **315**	**1.53** **1.19**	**13.1 **** **11.6 ****	**7**	**2**
[15]	1.5-2.2	50-170	3-6.5	NA	9	3
[16]	1.55-2.1	40-120	4.5-6.0	NA	10	4
[18]	3-5.6	33-45	3.1	NA	6	2
[19]	2.9-3.5	134-402	1-3	NA	8	2
[21]	0.669-1.215	140-644	1-2	NA	6	3

*: This work.
**: Same return-loss level using compensable coupling mechanism

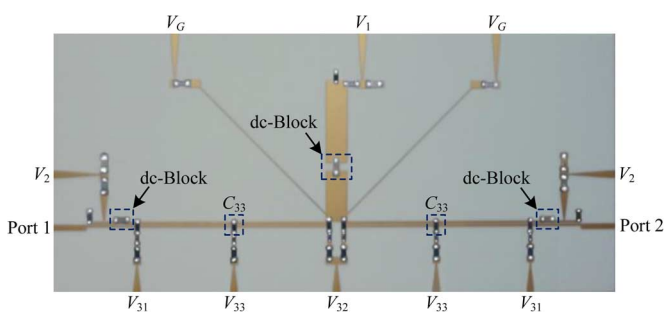

Fig. 21. Fabrication of the proposed tunable bandpass filter (i.e., Filter II). ($g = 0.15$ mm, $l_1 = 48.2$ mm, $l_{21} = 10$ mm, $l_{22} = 16.15$ mm, $w_1 = 0.45$ mm, and $w_2 = 4.2$ mm.)

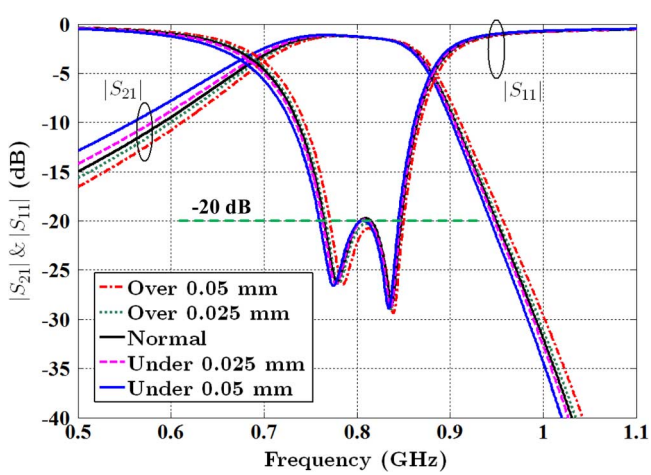

Fig. 22. Measured sensitivity to etching tolerances for the proposed tunable bandpass filter (i.e., Filter II) with narrow passband responses. (For all the cases, $V_1 = 3.1$ V, $V_2 = 10$ V, $V_{31} = 28$ V, and $V_{32} = 9$ V. Red line (in online version): $V_{33} = 3$ V; Green line (in online version): $V_{33} = 5$ V; Black line: $V_{33} = 7.2$ V; Pink line (in online version): $V_{33} = 10$ V; and Blue line (in online version): $V_{33} = 20$ V.)

tunable bandpass filter (i.e., Filter II) is implemented and fabricated as shown in Fig. 21. The dielectric substrate Rogers 4350B with thickness $h = 0.508$ mm and $\epsilon_r = 3.66$ is used. Similar to Filter I, three dc blocks are utilized to isolate the varators, which are adjusted by six dc voltages (i.e., V_1, V_2, V_{31}, V_{32}, V_{33}, and V_G). The BB857 varactors C_1, C_2, C_{31}, and C_{32} with dc voltage circuits are implemented the same as in Filter I. Note that there is an additional pair of varactors C_{33} (i.e., SMV2202-040LF) identically embedded at the center positions of the left and right PCMLs. To show the sensitivity

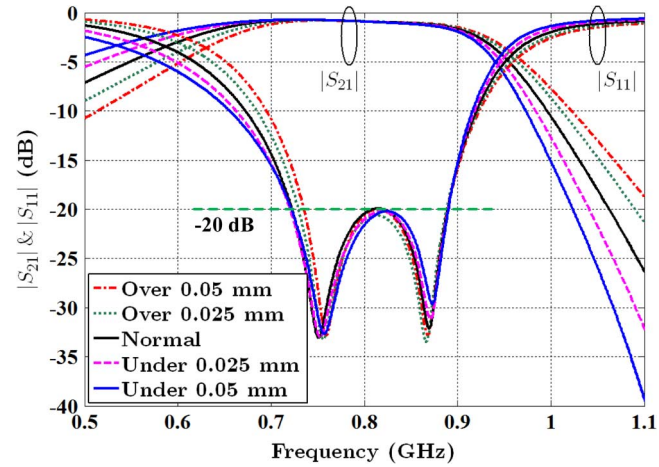

Fig. 23. Measured sensitivity to etching tolerances for the proposed tunable bandpass filter (i.e., Filter II) with wide passband responses. (For all the cases $V_1 = 13.5$ V, $V_2 = 11$ V, $V_{31} = 10$ V, and $V_{32} = 28$ V. Red line (in online version): $V_{33} = 0$ V; Green line (in online version): $V_{33} = 1$ V; Black line: $V_{33} = 4.5$ V; Pink line (in online version): $V_{33} = 10$ V; and Blue line (in online version): $V_{33} = 17$ V.)

of etching tolerances for Filter II, the masks are modified during the fabrication process because printed circuit board (PCB) factories cannot change the processing parameters to match the study extent of this paper. Figs. 22 and 23 present the measured responses (i.e., wide and narrow passband) of the proposed filters (i.e., Filter II) versus etching error, i.e., from over-etching 0.05 mm (2 mil) to under-etching 0.05 mm (2 mil), to demonstrate the sensitivity, respectively. From the measurements, two interesting functions about the existing of varactor C_{33} can be concluded as follows: 1) the return loss of the passband can be enhanced to 20 dB, which implies a better impedance matching with the varactor compensation and 2) reasonably small discrepancies of frequency responses due to the etching error are achieved.

IV. CONCLUSION

A novel tunable bandpass filter structure, which is based on a $\lambda/2$ resonator with a tapped open-stub in the middle, allows for both the two transmission poles and coupling strength tuning using only tuning elements attached to the filter. The center frequency and bandwidth of this structure can be easily tuned and the coupling weakened by tuning the poles can also be compensated by the tuning varactors between the coupled lines. The effect of the varactors has been theoretically analyzed in detail. Two second-order microstrip tunable filters have been designed, implemented, and measured. The passbands with different center frequencies, but nearly the same bandwidth and coupling strength, have been successfully realized in practice. Meanwhile, less sensitivity to fabrication tolerances of the frequency response can be achieved. This simple yet effective design can be useful for modern reconfigurable wireless communication systems.

APPENDIX A

To derive the $ABCD$-matrix of the model, as illustrated in Fig. 24(a), the four-port network shown in Fig. 24(b) is introduced. From the boundary condition of the port voltages and

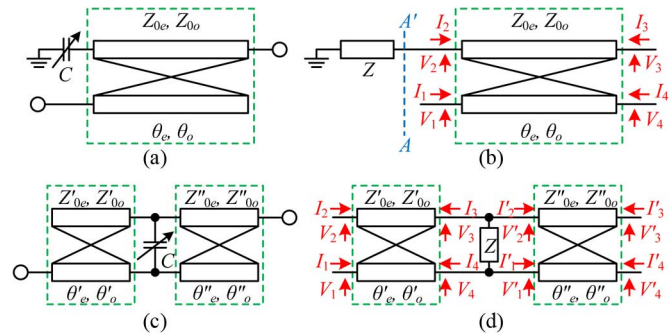

Fig. 24. Varactor-loaded PCMLs. (a) Series varactor-loaded PCML. (b) Four-port network of series varactor-loaded PCML. (c) Emebedded varactor-loaded PCML. (d) Four-port network of emebedded varactor-loaded PCML.

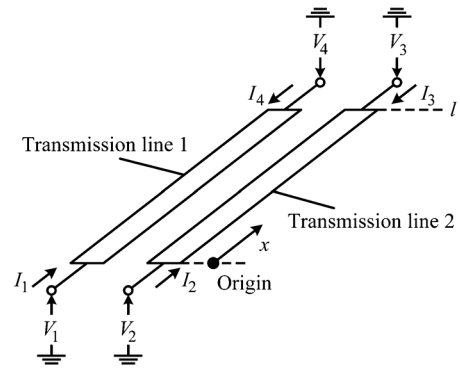

Fig. 25. Transmission-line model of the PCML.

currents, the relationship at the reference plane A–A′ can be expressed as

$$V_2 = I_2 Z. \tag{24}$$

Meanwhile, for the open-circuited boundary at port 4, the current $I_4 = 0$. Therefore, from the $ABCD$-matrix definition as follows:

$$\begin{bmatrix} V_1 \\ I_1 \end{bmatrix} = \begin{bmatrix} A & B \\ C & D \end{bmatrix} \begin{bmatrix} V_3' \\ I_3' \end{bmatrix}. \tag{25}$$

The $ABCD$-matrix can then be calculated as

$$A = \frac{a_{11}^2 - a_{12}^2 - Za_{11}c_{11} + Zc_{12}a_{12}}{Zc_{12} - a_{12}} \tag{26}$$

$$B = -\frac{a_{11}b_{11} - a_{12}b_{12} + Zb_{12}c_{12} - Za_{11}^2}{Zc_{12} - a_{12}} \tag{27}$$

$$C = \frac{a_{11}c_{11} - a_{12}c_{12} - Zc_{11}^2 + Zc_{12}^2}{Zc_{12} - a_{12}} \tag{28}$$

$$D = -\frac{b_{11}c_{11} - a_{12}^2 + Za_{12}c_{12} - Za_{11}c_{11}}{Zc_{12} - a_{12}} \tag{29}$$

where $Z = -j/\omega C$, and the parameters of a_{ii}, b_{ii}, c_{ii}, and d_{ii} can be found in Appendix B.

The $ABCD$-matrix of the embedded varactor-loaded PCML, as illustrated in Fig. 24(c), can be derived from the following boundary condition and current definition depicted in Fig. 24(d) as follows:

$$V_3 = V_2' \tag{30}$$

$$V_4 = V_1' \tag{31}$$

$$V_3 - V_4 = Z\left(I_4 + I_1'\right) = -Z\left(I_3 + I_2'\right) \tag{32}$$

$$I_2 = I_4' = 0. \tag{33}$$

Considering the similar process of the derivation, the $ABCD$-matrix of this model is not listed here.

Appendix B

The transmission line model of the conventional PCML is depicted in Fig. 25. The terminal behavior of such a four-port network has been investigated by [27] and the chain matrix is shown as follows:

$$\begin{bmatrix} V_1 \\ V_2 \\ I_1 \\ I_2 \end{bmatrix} = \begin{bmatrix} a_{11} & a_{12} & b_{11} & b_{12} \\ a_{21} & a_{22} & b_{21} & b_{22} \\ c_{11} & c_{12} & d_{11} & d_{12} \\ c_{21} & c_{22} & d_{21} & d_{22} \end{bmatrix} \begin{bmatrix} V_4 \\ V_3 \\ -I_4 \\ -I_3 \end{bmatrix} \tag{34}$$

where

$$a_{11} = a_{22} = d_{11} = d_{22} = \frac{1}{2}(\cos\theta_e + \cos\theta_o) \tag{35}$$

$$a_{12} = a_{21} = d_{12} = d_{21} = \frac{1}{2}(\cos\theta_e - \cos\theta_o) \tag{36}$$

$$b_{11} = b_{22} = \frac{j}{2}(Z_{0e}\sin\theta_e + Z_{0o}\sin\theta_o) \tag{37}$$

$$b_{12} = b_{21} = \frac{j}{2}(Z_{0e}\sin\theta_e - Z_{0o}\sin\theta_o) \tag{38}$$

$$c_{11} = c_{22} = \frac{j}{2}(Y_{0e}\sin\theta_e + Y_{0o}\sin\theta_o) \tag{39}$$

$$c_{12} = c_{21} = \frac{j}{2}(Y_{0e}\sin\theta_e - Y_{0o}\sin\theta_o) \tag{40}$$

where Z_{0e} and Z_{0o} are even- and odd-mode characteristic impedances, Y_{0e} and Y_{0o} are even- and odd-mode characteristic admittances, and

$$\theta_{e,o} = \beta_{e,o} l = \frac{\pi}{2}\frac{f}{f_{0e,o}} \tag{41}$$

are even- and odd-mode electrical lengths of the coupled lines, respectively.

Acknowledgment

The authors would like to thank the Huawei Technologies Company Ltd., for their support. The authors would also like to highlight the contribution of author R. B. Staszewski for his detail grammar checking of this paper's manuscript.

References

[1] I. C. Hunter and J. D. Rhodes, "Electronically tunable microwave bandstop filters," *IEEE Trans. Microw. Theory Techn.*, vol. MTT-30, no. 9, pp. 1361–1367, Sep. 1982.

[2] S. R. Chandler, I. C. Hunter, J. G. Gardiner, and J. G, "Active varactor tunable microwave filters," in *23rd Eur. Microw. Conf.*, Oct. 1993, pp. 244–245.

[3] B. W. Kim and S. W. Yun, "Varactor-tuned combine bandpass filter using step-impedance microstrip lines," *IEEE Trans. Microw. Theory Techn.*, vol. 52, no. 4, pp. 1279–1283, Apr. 2004.

[4] B. E. Carey-Smith and P. A. Warr, "Broadband-configurable bandstop-filter design employing a composite tuning mechanism," *IET Microw., Antenna, Propag.*, vol. 1, no. 2, pp. 420–426, Apr. 2007.

[5] B. E. Carey-Smith and P. A. Warr, "Broadband configurable bandstop filter with composite tuning mechanism," *Electron. Lett.*, vol. 40, no. 25, pp. 1587–1589, Dec. 2004.

[6] C. Rauscher, "Reconfigurable bandpadd filter with a three-to-one switchable passband width," *IEEE Trans. Microw. Theory Techn.*, vol. 51, no. 2, pp. 573–577, Feb. 2003.

[7] L. Zhu, V. Devabhaktuni, C. Wang, and M. Yu, "Adjustable bandwidth filter design based on interdigital capacitors," *IEEE Microw. Wireless Compon. Lett.*, vol. 18, no. 1, pp. 16–18, Jan. 2008.

[8] A. Miller and J.-S. Hong, "Wideband bandpass filter with reconfigurable bandwidth," *IEEE Microw. Wireless Compon. Lett.*, vol. 20, no. 1, pp. 28–30, Jan. 2010.

[9] L. Athukorola and D. Budimir, "Compact second-order highly linear varactor-tuned dual-mode filters with constant bandwidth," *IEEE Trans. Microw. Theory Techn.*, vol. 59, no. 9, pp. 2214–2220, Sep. 2011.

[10] C.-K. Liao, C.-Y. Chang, and J. Lin, "A reconfigurable filter based on doublet configuration," in *IEEE MTT-S Int. Microw. Symp. Dig.*, Jul. 2007, pp. 1607–1610.

[11] Y.-H. Chun and J.-S. Hong, "Electronically reconfigurable dual-mode microstrip open-loop resonator filter," *IEEE Microw. Wireless Compon. Lett.*, vol. 18, no. 7, pp. 449–451, Jul. 2008.

[12] W. Tang and J.-S. Hong, "Varactor-tuned dual-mode bandpass filters," *IEEE Trans. Microw. Theory Techn.*, vol. 58, no. 8, pp. 2213–2219, Jul. 2010.

[13] W.-H. Tu, "Compact low-loss reconfigurable bandpass filter with switchable bandwidth," *IEEE Microw. Wireless Compon. Lett.*, vol. 20, no. 4, pp. 208–210, Apr. 2010.

[14] M. S. Renedo, R. G. Garcia, J. I. Alonso, and C. B. Rodriguez, "Tunable combline filter with continuous control of center frequency and bandwidth," *IEEE Trans. Microw. Theory Techn.*, vol. 52, no. 1, pp. 191–199, Jan. 2005.

[15] Y.-C. Chiou and G. M. Rebeiz, "A tunable three-pole 1.5–2.2-GHz bandpass filter with bandwidth and transmission zero control," *IEEE Trans. Microw. Theory Techn.*, vol. 59, no. 11, pp. 2872–2878, Nov. 2011.

[16] Y.-C. Chiou and G. M. Rebeiz, "Tunable 1.55–2.1 GHz 4-pole elliptic bandpass filter with bandwidth control and $>$50 dB rejection for wireless systems," *IEEE Trans. Microw. Theory Techn.*, vol. 61, no. 1, pp. 117–124, Jan. 2013.

[17] T. Yang and G. M. Rebeiz, "Three-Pole 1.3–2.4-GHz diplexer and 1.1–2.45-GHz dual-band filter with common resonator topology and flexible tuning capabilities," *IEEE Trans. Microw. Theory Techn.*, vol. 61, no. 10, pp. 3613–3624, Oct. 2013.

[18] H. Joshi, H. H. Sigmarsson, S. Moon, D. Peroulis, and W. J. Chappell, "High-Q fully reconfigurable tunable bandpass filters," *IEEE Trans. Microw. Theory Techn.*, vol. 57, no. 12, pp. 3525–3533, Dec. 2009.

[19] A. Lacorte Caniato Serrano, F. Salete Correra, T.-P. Vuong, and P. Ferrari, "Synthesis methodology applied to a tunable patch filter with independent frequency and bandwidth control," *IEEE Trans. Microw. Theory Techn.*, vol. 60, no. 3, pp. 484–493, Mar. 2012.

[20] H.-J. Tsai, N.-W. Chen, and S.-K. Jeng, "Reconfigurable bandpass filter with separately relocatable passband edge," *IEEE Microw. Wireless Compon. Lett.*, vol. 22, no. 11, pp. 559–561, Nov. 2012.

[21] J.-R. Mao, W.-W. Choi, K.-W. Tam, W. Q. Che, and Q. Xue, "Tunable bandpass filter design based on external quality factor tuning and multiple mode resonators for wideband applications," *IEEE Trans. Microw. Theory Techn.*, vol. 61, no. 7, pp. 2574–2584, Jul. 2013.

[22] L. Zhu, S. Sun, and W. Menzel, "Ultra-wideband (UWB) bandpass filtersusing multiple-mode resonator," *IEEE Microw. Wireless Compon. Lett.*, vol. 15, no. 11, pp. 796–798, Sep. 2005.

[23] X. Luo *et al.*, "Wideband bandpass filter with wide stopband using loaded BCMC stub and short-stub," *IEEE Microw. Wireless Compon. Lett.*, vol. 21, no. 7, pp. 353–355, Jul. 2011.

[24] J.-S. Hong and M. J. Lancaster, *Microstrip Filters for RF/Microwave Applications*, 2nd ed. New York, NY, USA: Wiley, 2011.

[25] G. L. Mattheal, E. M. T. Johes, and L. Young, *Microstrip Filters, Impedance-Matching Networks, Coupling Structures*. Norwood, MA, USA: Artech House, 1980.

[26] L. Zhu and K. Wu, "Accurate circuit model of interdigital capacitor and its application to design of new quasi-lumped miniaturized filters with suppression of harmonic resonance," *IEEE Trans. Microw. Theory Techn.*, vol. 48, no. 3, pp. 347–356, Mar. 2000.

[27] R. K. Mongia, I. J. Bahl, P. Bhartia, and J.-S. Hong, *RF and Microwave Coupled-Line Circuits*, 2nd ed. Norwood, MA, USA: Artech House, 2007.

[28] C.-H. Liang, C.-H. Chen, and C.-Y. Chang, "Fabrication-tolerant microstrip quarter-wave stepped-impedance resonator filter," *IEEE Trans. Microw. Theory Techn.*, vol. 57, no. 5, pp. 1163–1172, May 2009.

[29] X. Luo *et al.*, "Compact ultra-wideband (UWB) bandpass filter with ultra-narrow dual-and quad-notched bands," *IEEE Trans. Microw. Theory Techn.*, vol. 59, no. 6, pp. 1509–1519, Jun. 2011.

Xun Luo (S'08–M'11–SM'12) was born in Sichuan, China, 1985. He received the B.E. degree (with highest honors) and Ph.D. degree (with highest honors) in electronic engineering from the University of Electronic Science and Technology of China (UESTC), Chengdu, China, in 2005 and 2011, respectively.

From 2002 to 2005 and 2006 to 2008, he was with the Chengdu Sine Science and Technology Ltd., as the Deputy Team-Leader of microwave wideband front-end R&D projects. From 2005 to 2006, he was with the 802nd Research Institute, Shanghai Academy of Spaceflight Technology (SAST), where he was involved with a project of microwave receivers for space communication. In 2007, he was with Philips Research East-Asia, Shanghai, China, where he developed the radio front-end of multi-mode/multi-card mobile systems. From 2010 to 2013, he was with the Huawei Technologies Company Ltd., as a Senior Researcher and then General Project Manager (PI) to lead the research and development of multi-bands P2P microwave/millimeter-wave systems-on-chip (SoCs), systems, and standards for back-haul communication. Since July 2013, he has been witht Electronics Research Laboratory, Delft University of Technology, Delft, The Netherlands. Since 2014, he has been a Huawei Chair-Consult. He has authored or coauthored over 30 journal and conference papers. He has filed/holds 18 patents in communication fields. His research interests include terabits-wireless transmission, multi-bands backhaul systems, digital-assisted microwave/millimeter-wave/terahretz transceivers, and system-in-package (SIP) research and development.

Dr. Luo is a member of the IEEE Microwave Theory and Techniques Society (IEEE MTT-S) Editorial Review Board. He was the recipient of a 2008 Huawei Scholarship, a 2009 Intel Fellowship, a 2009 Rohde & Schwarz Scholarship, and a 2010 Mediatek Scholarship, respectively. He was the recipient of the 2011 Huawei Transmission Network Research and Development Advanced Technology Achievement Award (First Place), the Huawei Distinguished Young Engineer Award in 2011 and 2012, and the Huawei President Award in 2013. He was also the recipient of the 2013 Sichuan Province Outstanding Doctoral Dissertations Award, China.

Sheng Sun (S'02–M'07–SM'12) was born in Shanxi, China, 1980. He received the B.Eng. degree in information engineering from Xi'an Jiaotong University, Xi'an, China, in 2001, and the Ph.D. degree in electrical and electronic engineering from Nanyang Technological University, Singapore, in 2006.

From 2005 to 2006, he was with the Institute of Microelectronics, Singapore. From 2006 to 2008, he was with Nanyang Technological University, Singapore. From 2008 to 2010, he was a Humboldt Research Fellow with the Institute of Microwave Techniques, University of Ulm, Ulm, Germany. Since 2010, he has been a Research Assistant Professor with the Department of Electrical and Electronic Engineering, The University of Hong Kong. He has authored or coauthored over 100 journal and conference publications. He coauthored *Microwave Bandpass Filters for Wideband Communications* (Wiley, 2012). His research interests include electromagnetic theory and

computational mathematics, multi-physics, numerical modeling of planar circuits and antennas, microwave passive and active devices, as well as microwave and millimeter-wave beamforming techniques.

Dr. Sun was the recipient of the Outstanding Reviewer Award of the IEEE MICROWAVE AND WIRELESS COMPONENTS LETTERS in 2010. He has been an associate editor for the *IEICE Transactions on Electronics* since 2010. He was the recipient of the General Assembly Young Scientists Award of the International Union of Radio Science (URSI) in 2014, the Hildegard Maier Research Fellowship of the Alexander Von Humboldt Foundation (Germany), in 2008, and the ISAP Young Scientist Travel Grant (Japan), in 2004.

Robert Bogdan Staszewski (M'97–SM'05–F'09) received the B.S.E.E. (*summa cum laude*), M.S.E.E., and Ph.D. degrees from the University of Texas at Dallas, Dallas, TX, USA, in 1991, 1992, and 2002, respectively.

From 1991 to 1995, he was with Alcatel Network Systems, Richardson, TX, USA, where he was involved with Sonet cross-connect systems for fiber-optics communications. In 1995, he joined Texas Instruments Incorporated, Dallas, TX, USA, where he was elected a Distinguished Member of Technical Staff (2% of the technical population). From 1995 to 1999, he was engaged in advanced CMOS read channel development for hard disk drives. In 1999, he co-started the Digital RF Processor (DRP) Group, Texas Instruments Incorporated, with a mission to invent new digitally intensive approaches to traditional RF functions for integrated radios in deep-submicrometer CMOS processes. Since July 2009, he has been a Professor with the Delft University of Technology, Delft, The Netherlands. He has authored or coauthored one book, two book chapters, and 150 journal and conference publications. He holds 110 U.S. patents. His research interests include nanoscale CMOS architectures and circuits for frequency synthesizers, transmitters, and receivers.

Dr. Staszewski currently serves on the Technical Program Committees (TPCs) of IEEE conferences: RFIC, ESSCIRC, and RFIT. He was a corecipient of the 2013 Best Paper Award of the IEEE RFIC Symposium and the 2011 Best Paper Award of the IEEE RFIT Symposium. He was also the recipient of the IEEE Circuits and Systems Industrial Pioneer Award.